Theoretical Studies on Nanocrystalline Diamond: Nucleation by Dicarbon and Electronic Structure of Planar Defects

Dieter M. Gruen,[†] Paul C. Redfern,[†] David A. Horner,[†,‡] Peter Zapol,[†] and Larry A. Curtiss*,[†]

Materials Science and Chemistry Divisions, Argonne National Laboratory, 9700 S. Cass Avenue, Argonne, Illinois 60439, and North Central College, P.O. Box 3063, Naperville, Illinois 60566

Density functional theory and ab initio molecular orbital theory have been used to calculate the energetics of C_2 insertion into C_9H_{12} and C_9H_{14} clusters that model unhydrided and monohydrided (100) diamond surfaces, respectively. The reaction of C_2 with either the C_9H_{12} or C_9H_{14} cluster is exothermic by more than 100 kcal/mol, but the lowest energy product is different for the two clusters. The reaction of singlet C_2 with the $C{=}C$ double bond of the C_9H_{12} cluster leads to either carbene structures or a cyclobutyne-like structure, with the former having the lower energy at both the HF/6-31G* and B3LYP/6-31G* levels of theory. No barrier for insertion into the $C{=}C$ double bond of the C_9H_{12} cluster was found at the HF/6-31G* and B3LYP/6-31G* levels of theory. The reaction of singlet C_2 with the HC−CH single bond or C−H bonds of the C_9H_{14} cluster leads to a structure having a cyclobutene-like geometry. We propose that the disparate nucleation rates of diamond crystallites grown in hydrogen-rich vs hydrogen-poor C_{60}/Ar microwave plasmas are accounted for qualitatively by these results. The carbon dimer, C_2, is a possible growth or nucleation species produced by fragmentation of C_{60}. Periodic density functional calculations of the electronic structure of a simple model of an sp^2-bonded diamond grain boundary show that π-bonded planar defects introduce new electronic bands into the fundamental band gap of diamond.

I. Introduction

Diamond films grown via chemical vapor deposition (CVD) are materials of enormous potential utility in fields such as tool and seal coatings, optical windows, surface acoustic wave devices, electrochemical electrodes, conformal coatings for microelectromechanical systems, and electron-emitting surfaces for flat-panel displays.[1] Each of these applications requires the diamond to be optimized for a different property, such as hardness, surface smoothness, optical transparency, electrical conductivity, or field emission. In principle, the optimization must be achieved by operating on the diamond microstructure, e.g., crystallite orientation or crystallite size. For example, in phase-pure diamond films, a drastic change in electrical conductivity is observed with reduction in crystallite size, with the material going from an insulator to an electrical conductor. This phenomenon is largely due to the fact that grain boundary carbon is π-bonded.[2] The grain boundaries are therefore conducting, and because their numbers vastly increase with decreasing crystallite size, the entire film becomes electrically conducting.

In contradistinction to diamond films grown by the traditional method involving CH_4/H_2 mixtures, where micrometer-size crystallites typically constitute the microstructure of the films, diamond grown from argon plasmas containing carbon is characterized by a microstructure consisting of crystallites with an average size of 3−10 nm.[3] This nanocrystalline diamond can be grown to thicknesses of at least 30 μm from argon/fullerene or argon/methane microwave plasmas.[1] A major advance was achieved recently when it was discovered that diamond crystallite size can be controlled continuously and reproducibly from the micrometer to the nanometer size by the addition of Ar to CH_4/H_2 microwave plasmas.[4]

The observed variations in crystallite size are presumably due to differences in the nucleation rates. From the relationship nucleation rate (cm^{-2} s^{-1}) = growth rate (cm s^{-1}) × crystallite volume (cm^{-3}), one finds that a growth rate of 1 μm/h for crystallite sizes of 1 μm and 15 nm yields nucleation rates of ca. 10^4 and 10^{10} cm^{-2} s^{-1}, respectively. We distinguish between the regime of low secondary nucleation rates ($\sim 10^4$ cm^{-2} s^{-1}) observed with hydrogen-rich plasmas, which lead to micrometer-size crystallites with typically columnar growth morphology, and the regime of high secondary nucleation rates (10^{10} cm^{-2} s^{-1}) observed with argon plasmas containing carbon, resulting in randomly oriented nanocrystalline film morphologies.[5]

The two growth regimes also differ in the amount of dicarbon, C_2, present in the gas phase. Argon plasmas containing high concentrations of dicarbon produced by fragmentation of C_{60} or C_2H_2 molecules are intensely green due to emission of Swanband radiation.[6] The ground-state population of C_2 has recently been found by optical absorption spectroscopy to be in the range 10^8-10^{12} molecules/cm^3 depending on gas composition and plasma parameters, with low C_2 contents associated with high H_2 contents and high C_2 contents associated with low H_2 but high Ar content. In earlier papers,[7,8] we proposed a mechanism for the growth of nanocrystalline diamond films on the (110) surface which featured C_2 as the growth species in the virtual absence of hydrogen. Density functional calculations made for growth on the (110) surface showed that the individual steps in this growth mechanism are energetically very favorable and have small activation barriers.

It is likely that the (100) surface has a substantial fraction (0.1−1%) of sites devoid of hydrogen under the experimental conditions under which nanocrystalline diamond is obtained.

[†] Argonne National Laboratory.
[‡] North Central College.

The depositions are carried out with small amounts of hydrogen admixtures (1−2%), while the gas species present in overwhelming quantity is argon, which may act to remove some of the surface hydrogen, particularly at the substrate temperatures of 700−900 °C in which the depositions are carried out. The structures of both the unhydrided (bare) and monohydrided diamond (100) surfaces have been intensively investigated.[9] A detailed study, which reviews much of the earlier literature, concludes that both the bare and the monohydrided surfaces reconstruct to form dimer rows, yielding a 2 × 1 surface symmetry.[10] There appears to be general agreement that the dimers are π-bonded on the bare surface and σ-bonded on the monohydrided surface. It is also possible that a small fraction of carbon atoms on unhydrided portions of the surface exist as free radicals rather than reconstructing to form π-bonded dimers.

Clearly, the large renucleation rates observed in the synthesis of nanocrystalline diamond films make an inquiry of the secondary nucleation mechanism of considerable importance. In this paper, we present the results of a computational study of the energetics of the reactions of C_2 with small hydrocarbon clusters that model the initial steps of the reaction of C_2 with the unhydrided and monohydrided diamond (100) surfaces. From these results, we gain insight into the differences in reaction mechanisms with and without hydrogen present. The results obtained for the (100) surface are expected to be applicable to a wide range of diamond surfaces with higher Miller indices. The reason lies in the structural similarity between the (100) surface and the general case of a diamond surface. Indeed, for unhydrided and unreconstructed surfaces, there are always two broken bonds per surface carbon atom and, therefore, a trend to reconstruct by forming surface dimers connected via double bonds except for two special surfaces, i.e., (111) and (110), that have only one broken bond per surface atom. Random growth will result in no particular orientation of the film; thus, (100)-like orientations will dominate and the (100) surface is considered to be a model of a general surface in the studies of the nucleation mechanism.

In nanocrystalline diamond, several percent of the atoms are located at the interface between grains. Therefore, electronic and mechanical properties of the diamond material are largely controlled by grain boundaries. We present results of a periodic density functional calculation of a stacking fault that is a model for the diamond grain boundary with sp^2 bonding across the interface, from which we obtain information on structural and electronic properties of the system.

The theoretical methods used are described in section II. The results for the cluster models of the unhydrided and monohydrided (100) surfaces are presented in section III. The implications for nucleation rates of diamond crystallites grown in hydrogen-rich versus hydrogen-poor microwave plasmas are discussed in section IV. Finally, results from periodic calculations of the electronic structure of the sp^2-bonded diamond grain boundary are presented in section V.

II. Theoretical Methods

Energy calculations were carried out using ab initio molecular orbital theory[11,12] and density functional theory.[13] The ab initio calculations were carried out at the HF/6-31G*,[11] MP2/6-31G*,[11] and G2[14] levels of theory. The density functional calculations were carried out using the gradient-corrected B3LYP density functional methods with the 6-31G* basis (denoted B3LYP/6-31G*). Spin-restricted methods were used for calculations on singlet electronic states. For C_2, all calculations were done on the $^1\Sigma_g$ electronic state, although the low-
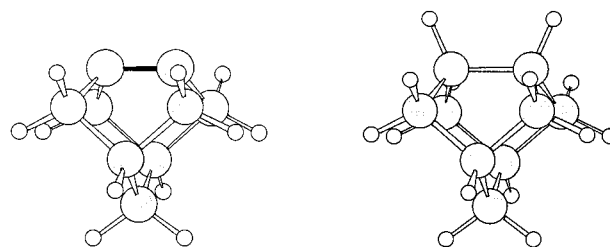

Figure 1. Illustration of the C_9H_{12} and C_9H_{14} clusters used to represent the unhydrided and monohydrided (100) reconstructed diamond surfaces, respectively.

lying $^3\Sigma_u$ state is also accessible at the ca. 1600 K temperatures typical of CVD experiments.

To study properties of the grain boundary in nanocrystalline diamond, we employed the periodic density functional method implemented in CRYSTAL95.[15] Bloch functions in this approach are constructed from the localized atomic orbitals, which are linear combinations of Gaussian orbitals. Becke exchange[16] and Perdew−Wang correlation[17] functionals were chosen for this study. To account for less diffuse functions in the crystalline environment, the standard 6-31G* basis set for carbon was modified by substituting a scaling factor of 1.1 for outer sp and d functions.

III. Carbon Dimer Insertion into Unhydrided and Monohydrided (100) Surfaces

An ethylene molecule and a C_9H_{12} molecule, illustrated in Figure 1, were used to model the carbon−carbon double bonds of the (100) unhydrided surface into which C_2 may insert. The HC−CH single bond on the monohydrided surface was modeled by an eclipsed ethane molecule as well as a C_9H_{14} molecule, also shown in Figure 1. The larger molecules provide the more realistic models for the surface, while the ethylene and ethane molecules permit the reliability of the B3LYP/6-31G* method for the bond insertion reactions to be assessed. For all calculations involving addition of C_2 to these models, the atom positions were allowed to relax fully. The only exceptions were studies of the barriers to the insertion of C_2 into C=C and HC−CH bonds, where a C_{2v} constraint was placed on the insertion reactions, and the G2 calculations, which are carried out at MP2 geometries by definition.

A. Unhydrided (100) Surface. The reaction of singlet C_2 with the double bond of ethylene leads to cyclopropylidenecarbene (**1** and **2**) or cyclobutyne (**3**). The structures are illustrated in Figure 2. The total energies of these structures are given in Table 1 at the four levels of theory used in this work. The relative energies are given in Table 2. At the HF/6-31G* level, the cyclopropylidenecarbene has a C_{2v} structure (**1**), while at the higher levels of theory it has a C_s structure (**2**) with the inserted C_2 tilted. Cyclobutyne [structure **3**] is a saddle point at the HF/6-31G* and B3LYP/6-31G* levels of theory, and a local minimum at the MP2(full)/6-31G* level of theory. It is 25.4 kcal/mol less stable than the tilted cyclopropylidenecarbene (**2**) at the G2 level of theory, while the B3LYP/6-31G* calculation gives an energy difference of 28.5 kcal/mol. Although the B3LYP/6-31G* and G2 methods agree well on the relative energies of structures **2** and **3**, they are in poorer agreement concerning the energy of the reaction $C_2 + C_2H_4 \rightarrow C_4H_4$ (**2**), for which the reaction energies are −108 and −81 kcal/mol, respectively. Several other studies[18,19] have reported structures for these two species. Skell et al.[18] found that at the HF/3-21G level, cyclopropylidenecarbene is 23.3 kcal/mol more stable than cyclobutyne, which is consistent with our results. Johnson and

Theoretical Studies on Nanocrystalline Diamond

J. Phys. Chem. B, Vol. 103, No. 26, 1999 **5461**

TABLE 1: Total Energies (E_e) of $C_2(^1\Sigma_g^+)$, C_2H_4, and Products[a]

structure	state	symmetry	HF/6-31G*	MP2(full)/6-31G*	B3LYP/6-31G*	G2
1	$^1A_1$	C_{2v}	−153.62715 (0)	−154.12939 (1)	−154.64740 (1)	−154.40320
2	$^1A'$	C_s		−154.13982 (0)	−154.64856 (0)	−154.40747
3	$^1A_1$	C_{2v}	−153.55165 (2)	−154.10231 (0)	−154.60214 (1)	−154.37013
C_2	$^1\Sigma_g^+$	$D_{\infty h}$	−75.37903 (0)	−75.70462 (0)	−75.88240 (0)	−75.80664
C_2H_4	^1A_g	D_{2h}	−78.03172 (0)	−78.29429 (0)	−78.58746 (0)	−78.46483

[a] Energies in hartrees. Values in parentheses are the number of imaginary frequencies. Structures shown in Figure 2.
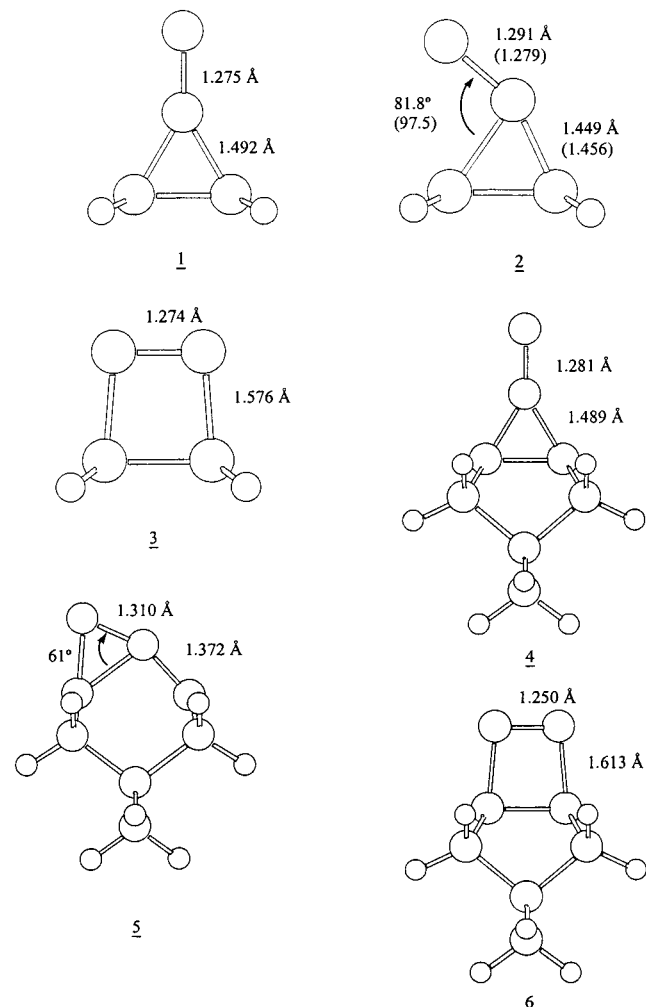

1

2

3

4

5

6

Figure 2. Optimized structures of products resulting from insertion of a C_2 molecule into the carbon−carbon double bond of ethylene and the C_9H_{12} cluster.

TABLE 2: Relative Energies of $C_2(^1\Sigma_g^+)$ + C_2H_4 and Products[a]

structure	HF/6-31G	MP2(full)/6-31G*	B3LYP/6-31G*	G2
$C_2 + C_2H_4$	0	0	0	0
1	−132.2			
2		−84.2	−108.4	−81.0
3	−85.4	−58.7	−79.9	−55.6

[a] Energies in kcal/mol. Includes zero-point vibrational energies.

Daoust[19] found similar results in calculations that included correlation energy. The absolute minimum on the potential energy surface corresponds to vinyl acetylene,[20] but this structure results from insertion of C_2 into a C−H bond of ethylene.

The reaction of singlet C_2 with the double bond of the C_9H_{12} cluster also leads to carbene structures (**4** and **5** in Figure 2) or a cyclobutyne-like structure (**6** in Figure 2), similar to the reaction with the double bond of ethylene. The total energies of these structures are given in Table 3 at the HF/6-31G* and

TABLE 3: Total (E_e) and Relative Energies of $C_2(^1\Sigma_g)$ + C_9H_{12} and Products[a]

	HF/6-31G*		B3LYP/6-31G*	
structure	E_e	rel. E	E_e	rel. E
$C_2(^1\Sigma_g)$ + C_9H_{12}	−423.06650	0	−425.96386	0
4	−423.33937 (0)	−171.2 [−168.1]	−426.18657 (1)	−139.8 [−137.0]
5			−426.20963 (0)	−154.2 [−150.5]
6	−423.28101 (2)	−134.6 [−132.0]	−426.15679 (1)	−121.1 [−118.3]

[a] Total energies in hartrees and relative energies in kcal/mol. Values in parentheses are the number of imaginary frequencies. Relative energies in square brackets include zero-point vibrational energy.

TABLE 4: Barriers to C_2 Insertion into the C=C Double Bond[a]

	HF/6-31G*	MP2/6-31G*	B3LYP/6-31G*	G2
$C_2 + C_2H_4 \rightarrow$ C_4H_4 (**1**)	0	0.6	0	0
$C_2 + C_9H_{12} \rightarrow$ $C_{11}H_{12}$ (**4**)	0		0	

[a] Energies in kcal/mol. Geometry is restricted to C_{2v} symmetry. For $C_2 + C_9H_{12} \rightarrow C_{11}H_{12}$ (**4**), HF/6-31G* geometries were used in MP2/6-31G* and B3LYP/6-31G* calculations.

B3LYP/6-31G* levels of theory. The relative energies are also given in this table. At the HF/6-31G* level, the carbene product has a C_{2v} structure (**4**), while at the B3LYP/6-31G* level of theory, it has a C_s structure (**5**) with the inserted C_2 tilted, similar to the ethylene result. The B3LYP/6-31G* reaction energy for $C_2 + C_9H_{12} \rightarrow C_{11}H_{12}$ (**5**) is −150 kcal/mol. The cyclobutyne-like structure (**6**) for the $C_{11}H_{12}$ cluster is about 30 kcal/mol higher in energy and is a saddle point at both levels of theory.

The barriers for insertion of the C_2 into the C=C double bond in ethylene and the C_9H_{12} cluster were investigated by constraining the C_2 to approach the ethylene or C_9H_{12} along a path that preserved C_{2v} symmetry, as in structures **1** and **5**. The barrier for ethylene was investigated at all four levels of theory, and with the exception of MP2/6-31G*, there was no barrier. However, at the MP2/6-31G* level the barrier was only 0.6 kcal/mol. No barrier for insertion into the C=C double bond of the C_9H_{12} cluster was found at the HF/6-31G* and B3LYP/6-31G* levels of theory. The results are summarized in Table 4.

B. Monohydrided (100) Surface. Reaction of singlet C_2 with eclipsed ethane occurs via insertion into either the HC−CH single bond or into C−H bonds. Insertion of C_2 into the HC−CH single bond yields dimethylvinylidene (**7**), while insertion into one or two C−H bonds produces ethylvinylidene (**8**) and cyclobutene (**9**), respectively. The structures are illustrated in Figure 3. The total energies of these structures are given in Table 5 at five levels of theory, and their relative energies are given in Table 6. The ethylvinylidene conformation (**8**) shown in Figure 3 has one imaginary frequency, corresponding to rotation of the methyl group about the C−C bond, but the analogous structure on the C_9H_{14} model surface has all real frequencies.
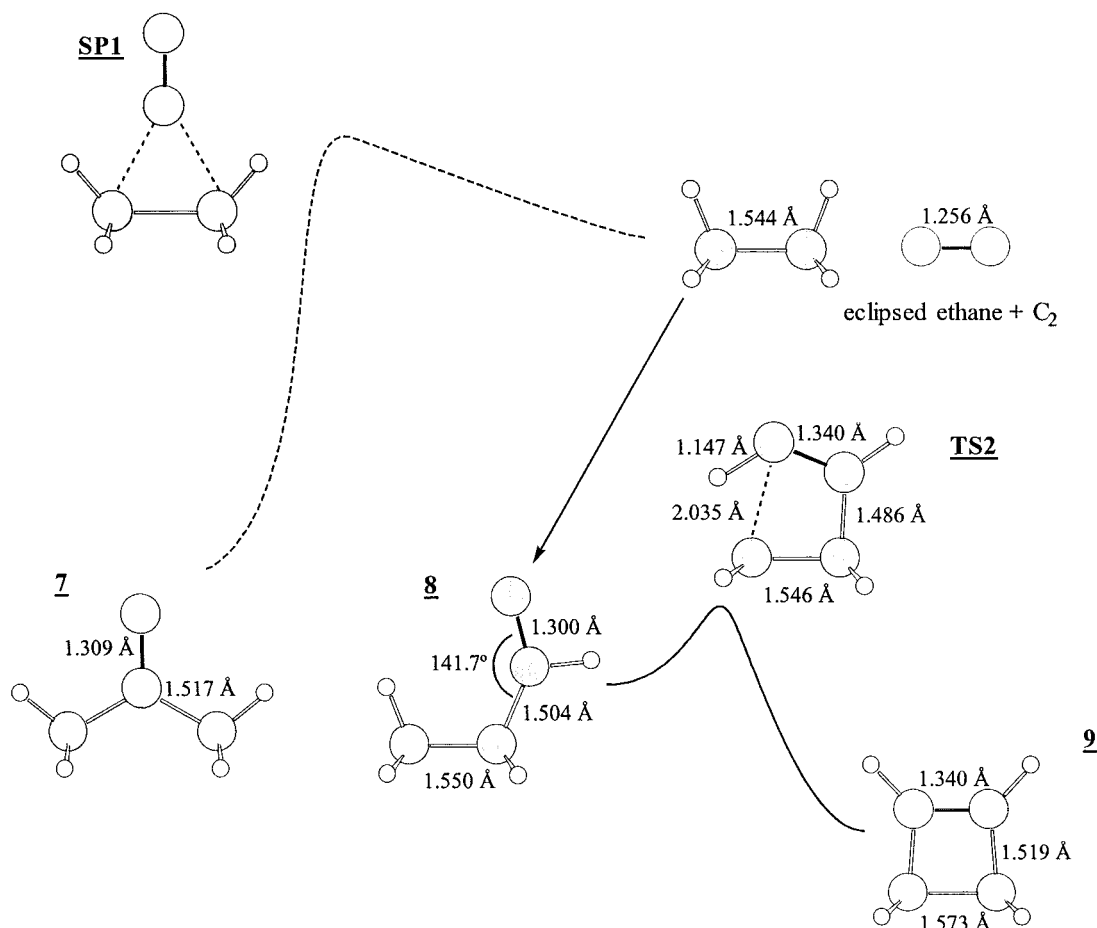
Figure 3. Reaction scheme for insertion of C_2 into the HC−CH or C−H bond of the eclipsed ethane. Relative energies are illustrated qualitatively by the vertical displacements. Equilibrium structures are labeled with numbers, transition states are labeled with numbers preceded by the letters TS, and saddle points having more than one imaginary frequency are labeled with numbers preceded by the letters SP. The geometries shown were obtained at the B3LYP/6-31G* level of theory.

TABLE 5: Total Energies[a] (E_e) of C_2($^1\Sigma_g^+$), Eclipsed C_2H_6, Products, and Transition States

structure[b]	state	symmetry	AM1	HF/6-31G*	MP2(full)/6-31G*	B3LYP/6-31G*	G2[c]
C_2	$^1\Sigma_g^+$	$D_{\infty h}$	0.34459 (0)	−75.37903 (0)	−75.70462 (0)	−75.88240 (0)	−75.80664
eclipsed C_2H_6	$^1A_1$	C_{2v}	−0.02582 (1)	−79.22400 (1)	−79.50397 (1)	−79.82593 (1)	−79.63123
7	$^1A_1$	C_{2v}	0.15786 (0)	−154.84110 (0)	−155.34380 (0)	−155.89778 (0)	−155.57367
8	$^1A'$	C_s	0.16030 (1)	−154.83016 (1)	−155.33874 (1)	−155.88637 (1)	−155.56844
9	$^1A_1$	C_{2v}	0.07282 (0)	−154.89962 (0)	−155.42933 (0)	−155.97326 (0)	−155.64388
SP1	$^1A_1$	C_{2v}	0.37149 (4)	−154.57017 (5)	−155.13095 (4)	−155.68536 (4)	−155.37950
TS2	$^1A'$	C_s	0.20530 (1)	−154.75118 (1)	−155.29546 (1)	−155.84905 (1)	−155.53129

[a] In hartrees. Values in parentheses are number of imaginary frequencies. [b] Structures are shown in Figure 3. [c] Includes zero-point vibrational energy.

TABLE 6: Relative Energies[a] of C_2 ($^1\Sigma_g^+$) + Eclipsed C_2H_6 and Products

structure[b]	AM1	HF/6-31G	MP2(full)/ 6-31G*	B3LYP/ 6-31G*	G2[c]
C_2 + eclipsed C_2H_6	0	0	0	0	0
7	−101.0	−149.4	−84.8	−118.9	−87.7
8	−99.4	−142.5	−81.7	−111.7	−84.4
9	−154.3	−186.1	−138.5	−166.2	−131.7
SP1	33.1	20.6	48.7	14.4	34.2
TS2	−71.2	−93.0	−54.5	−88.3	−61.1

[a] In kcal/mol. [b] Structures are shown in Figure 3. [c] Includes zero-point vibrational energy.

In contrast to the reaction of dicarbon with ethylene, the lowest energy product of the reaction of C_2 with eclipsed ethane is obtained from insertion into C−H bonds rather than the C−C bond. The G2 reaction energy of C_2 + C_2H_6 → product is −88 kcal/mol when the product is dimethylvinylidene (**7**), compared to −132 kcal/mol for a cyclobutene product (**9**). The B3LYP/ 6-31G* calculations yield a similar energy difference between dimethylvinylidene and cyclobutene, 47.3 kcal/mol, but give a C_2 + C_2H_6 → dimethylvinylidene reaction energy of −119 kcal/ mol, which is 31 kcal/mol more exothermic than that predicted by G2 theory.

The reaction of singlet C_2 with the HC−CH bond of the C_9H_{14} cluster leads to structures analogous to the products of the reaction of C_2 with eclipsed ethane, including carbene structures (**10** and **12** in Figure 4), a cyclobutene-like structure (**13** in Figure 4), and a cycloheptane-like structure (**11** in Figure 4). The total energies of these structures are given in Table 7 at the AM1, HF/6-31G*, and B3LYP/6-31G* levels of theory. The relative energies are also given in this table. The B3LYP/6- 31G* reaction energy for the insertion of one end of the dicarbon into the HC−CH bond, i.e., C_2 + C_9H_{14} → $C_{11}H_{14}$ (**10**), is −130

Theoretical Studies on Nanocrystalline Diamond

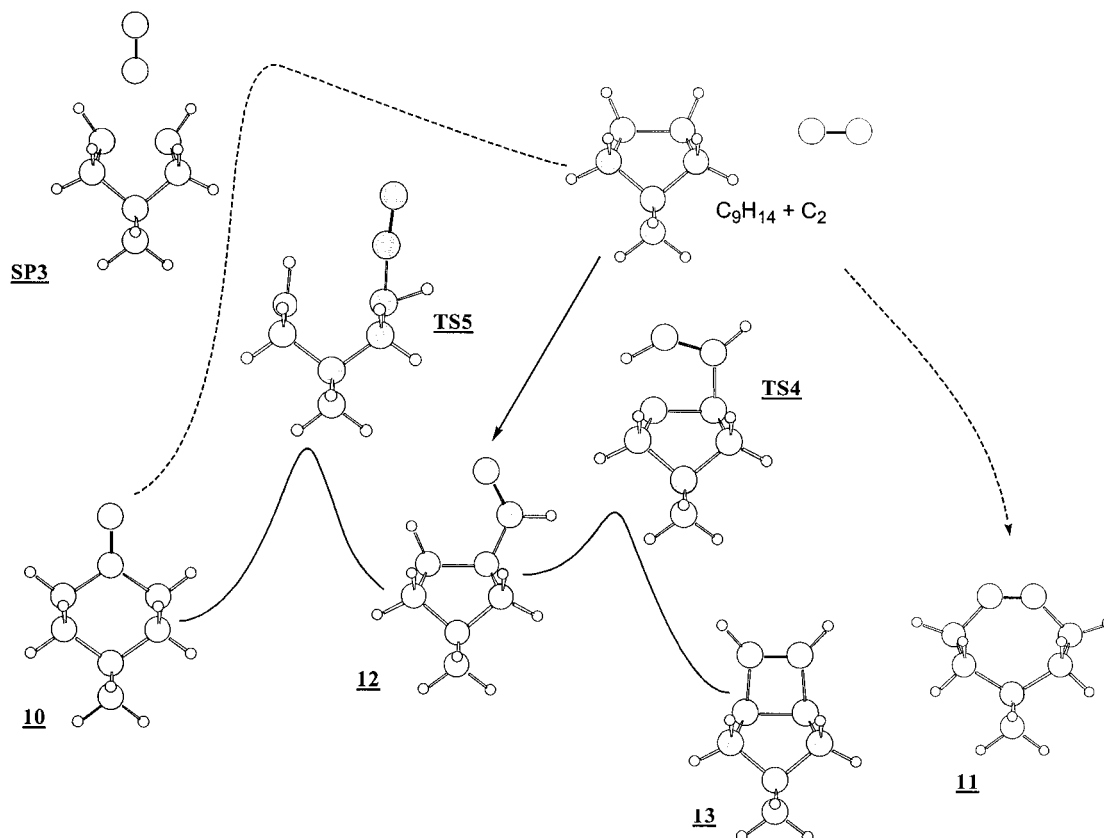*J. Phys. Chem. B, Vol. 103, No. 26, 1999* **5463**

Figure 4. Optimized structures of products resulting from insertion of C_2 into the HC–CH or C–H bond of the C_9H_{14} cluster. Relative energies are illustrated qualitatively by the vertical displacements. Equilibrium structures are labeled with numbers, transition states are labeled with numbers preceded by the letters TS, and saddle points having more than one imaginary frequency are labeled with numbers preceded by the letters SP. All geometries were obtained at the B3LYP/6-31G* level of theory.

TABLE 7: Total (E_e) and Relative Energies[a] of $C_2(^1\Sigma_g)$ + C_9H_{14} and Products

	AM1		HF/6-31G*		B3LYP/6-31G*	
structure[b]	E_e	rel. E	E_e	rel. E	E_e	rel. E
C_2 + C_9H_{14}	0.31687	0	−424.34910	0	−427.27353	0
10	0.12975	−117.4	−424.60505	−160.6	−427.48141	−130.4
11	0.12783	−118.6	−424.58621	−148.8	−427.48952	−135.5
12	0.16181	−97.3	−424.57984	−144.8	−427.45643	−114.8
13	0.09165	−141.3	−424.63539	−179.7	−427.53223	−162.3
SP3	0.35479	23.8	−424.33526	8.7	−427.27697	−2.2
TS4	0.21416	−64.5	−424.49575	−92.0	−427.41789	−90.6
TS5	0.30960	−4.6	−424.37671	−17.3	−427.30992	−22.8

[a] Total energies in hartrees and relative energies in kcal/mol. [b] Structures are shown in Figure 4.

TABLE 8: Barriers to C_2 Addition to C–C and C–H Bonds

	barrier height[a]				
reaction[b]	AM1	HF/6-31G*	MP2(full)/6–13G*	B3LYP/6-31G*	G2[c]
C_2+ C_2H_6 → C_4H_6 (8)	0	0			
C_4H_6 (8) → C_4H_6 (9)	28.2	49.6	27.2	23.4	23.3
$C_{11}H_{14}$ (12) → $C_{11}H_{14}$ (10)	92.7	127.5			
$C_{11}H_{14}$ (12) → $C_{11}H_{14}$ (13)	32.8	52.8		24.2	

[a] In kcal/mol. Geometry is restricted to C_{2v} symmetry for C_2 + C_2H_6 → C_4H_6 (7) and C_2 + C_9H_{14} → $C_{11}H_{14}$ (13). [b] Structures are shown in Figures 3 and 4. [c] Includes zero-point vibrational energy.

kcal/mol, about 11 kcal/mol more exothermic than the insertion of C_2 into the HC–CH bond of eclipsed ethane. The cyclobutene-like structure (13) for the $C_{11}H_{14}$ cluster is about 32 kcal/mol lower in energy than the carbene (10), consistent with the results for eclipsed ethane.

Ethylvinylidene (8) is an intermediate on the reaction path connecting C_2 + eclipsed ethane with cyclobutene (9). It is produced when dicarbon inserts into a single C–H bond of eclipsed ethane with no activation energy (see Table 8), releasing 84 kcal/mol at the G2 level of theory, similar to previous results for methane.[7] At the B3LYP/6-31G* level of theory, the reaction energy is −112 kcal/mol. In structure 8 the H atom bridges the two carbon atoms of C_2 at the MP2 level of theory but is bonded exclusively to the interior carbon at lower levels (as shown in Figure 3), including B3LYP/6-31G*. A similar situation exists with the product of C_2 insertion into a C–H bond of methane.[7] On the cluster model of the surface, the ethylvinylidene

analogue, $C_{11}H_{14}$ (12), is an intermediate on the path connecting C_9H_{14} + C_2 to the cyclobutene-like product (13) and lies 115 kcal/mol lower than C_9H_{14} + C_2 at the B3LYP/6-31G* level. We did not investigate the barrier for the insertion of dicarbon into the C–H bond of C_9H_{14}, but it is presumed to be equal to zero on the basis of the results for the addition of C_2 to eclipsed ethane. Table 8 also shows the results of calculations of the barrier for the insertion of the carbene end of ethylvinylidene (8) into a second C–H bond to yield cyclobutene (9). At the G2 level of theory, the transition state (TS2) lies 23 kcal/mol above ethylvinylidene. At the B3LYP level, the barrier height is 23 kcal/mol, slightly less than the 24 kcal/mol B3LYP barrier height for the corresponding reaction on the C_9H_{14} cluster.

We also investigated the barriers for insertion of the C_2 into the HC–CH bond of eclipsed ethane and the C_9H_{14} cluster to produce structures 7 and 10, respectively. The results are shown
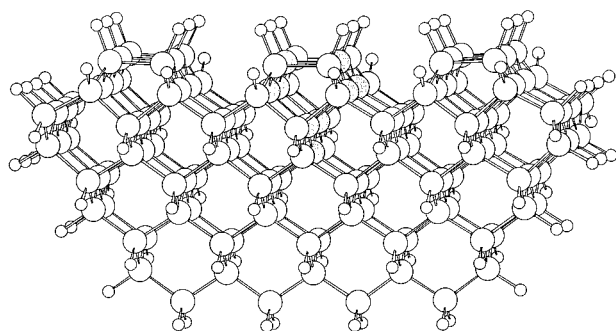
Figure 5. Geometry of the large diamond-like cluster used in single-point energy calculations. The shaded atoms show where the small clusters of Figures 1 and 4 were embedded.

in Table 8. In each case, the C_2 was constrained to lie along the C_{2v} reaction path while being removed in a stepwise manner from the C_2H_6 or C_9H_{14} moiety, while a geometry optimization was performed at each step. Although a maximum was found along the C_{2v} reaction path at each level of theory, no true transition states were obtained because the saddle point structures (**SP1** in Figure 3 and **SP3** in Figure 4) had more than one imaginary frequency. When geometry optimizations were performed along the previous reaction path, but with the symmetry constraint removed, the C_{2v} structures relaxed to the monosubstituted vinylidene geometry (**8** or **12**), which suggests that the insertion of C_2 into the HC−CH bond does not occur in a single step but rather via the monosubsituted vinylidene intermediate formed by the insertion of C_2 into a C−H bond. On the $C_{11}H_{14}$ cluster, a true transition state (**TS5**) connecting the mono- (**12**) and disubstituted (**10**) vinylidene structures was located 92 kcal/mol above the monosubstituted vinylidene at the B3LYP/6-31G* level, only 23 kcal/mol lower than C_2 + C_9H_{14}. The energies of the C_{2v} saddle points do establish upper bounds to the energy barrier for C_2 insertion into the HC−CH bond via any one-step path that may exist.

To examine the effects of the surrounding diamond crystal on the energies of the structures in Figure 4, structures **10**, **12**, and **13** were embedded in the 140-carbon cluster shown in Figure 5. The AM1 energies of these large structures were then determined by single-point energy calculations carried out at MM2 geometries. In all three cases, the AM1//MM2 reaction energies for the addition of C_2 to the 140-carbon cluster are slightly less negative than the AM1 reaction energies for the addition of C_2 to the 9-carbon cluster of Figure 4. Not surprisingly, the difference between large and small clusters increases as the geometry becomes less compact. The formation of **13** is 3.8 kcal/mol less exothermic on the 140-carbon cluster than on the 9-carbon cluster, while formation of **12** and **10** are 9.5 and 13.0 kcal/mol less exothermic, respectively, on the 140-carbon cluster.

IV. Discussion: Implications for Nucleation of Diamond Crystallites

Our calculations, which include correlation energy and geometry optimization, indicate that insertion of C_2 into a carbon−carbon double bond leads to a large energy lowering, at least 120 kcal/mol for a C_9H_{12} cluster. The insertion of a single end of the C_2 into a C=C bond to yield a carbene product (**4** or **5**) occurs with no energy barrier and is 33 kcal/mol more exothermic at the B3LYP/6-31G* level than the double insertion that yields a cyclobutyne-like structure (**6**). In contrast, the carbene product (**10**) produced by insertion of one end of C_2 into a C−C single bond on the C_9H_{14} cluster is 32 kcal/mol

higher in energy at the B3LYP/6-31G* level than the cyclobutene-like structure (**13**) produced by insertion of the C_2 into two C−H bonds. For both the carbene (**10**) and cyclobutene-like (**13**) products, the reaction paths from the C_2 and C_9H_{14} reactants involve the initial insertion of C_2 into a C−H bond to produce a common, monosubstituted vinylidene intermediate (**12**), but the energy barrier between this intermediate and the carbene product (**10**) is about 60 kcal/mol higher than the barrier along the path from (**12**) to the cyclobutene-like product.

These results suggest that the mechanism of diamond growth from dicarbon is quite dependent on the degree of hydrogenation of the reconstructed (100) surface. On the unhydrided surface, the most energetically favorable addition of C_2 is insertion of C_2 into a C=C bond to produce the carbene (**4** or **5**), while insertion of C_2 into C−H bonds to form the cyclobutene-like structure (**13**) is favored on the monohydrided surface. Starting from the cyclobutene-like structure, formation of a new layer of the existing monohydrided surface proceeds readily.[21] In contrast, the carbene (**4** or **5**) on the unhydrided surface may act as a nucleation site for a new diamond crystal. Because only a small fraction of the (100) surface sites are unhydrided, most C_2 insertion events likely lead to growth, with only a few leading to nucleation. Thus, we propose that the nucleation begins with the insertion of one end of the C_2 molecule into the π bonds of unhydrided portions of the reconstructed (100) surface of diamond, after which the unattached carbon atom can react with other C_2 molecules from the gas phase to nucleate a new diamond crystallite.

Since most of the diamond (100) surface dimers are hydrided under even hydrogen-poor experimental conditions, it is necessary to see if nucleation at unhydrided (100) dimers can account for the nucleation rates measured experimentally. It is reasonable to assume that secondary nucleation occurs primarily at (100)-like surfaces. The exposed faces of randomly oriented crystallites are usually (100)-like, because the face-centered cubic diamond lattice has only two sets of crystallographic planes, (111) and (110), having just one dangling bond per carbon atom; all other crystallographic planes share a common character with the (100) planes in that there are two dangling bonds per carbon atom before surface reconstruction. Also, in many cases, the diamond crystallites are observed to be cubic. When a diamond crystallite grows, the three principal growth directions are ⟨110⟩, ⟨111⟩, and ⟨100⟩. The ultimate crystal shape will be determined by the relative growth rates along the three directions, assuming secondary nucleation and growth takes place only after the growth of the parent crystallite is completed. When the growth rate ratios satisfy the conditions $v_{100}/v_{111} \leq 1/\sqrt{3}$ and $v_{100}/v_{110} \leq 1/\sqrt{2}$, where v is the growth rate or growth velocity, the ultimate shape of the crystallite will be a cube enclosed by (100) faces.[22] As already pointed out, density functional calculations have shown that the growth of diamond nanocrystallites can take place on the (110) faces, where a dimer can be inserted into a surface C−H bond with a low energy of activation.[8] As the growth rate along ⟨110⟩ directions is almost certainly much greater than that along ⟨100⟩ directions ($v_{110} \gg v_{100}$), this will result in the enlargement of the (100) surface area, which would in turn enhance the probability of secondary nucleation at this newly created (100) surface.

If we assume that secondary nucleation occurs only at the carbon dimers of reconstructed (100)-like surfaces, then the nucleation density is at most about 8 sites/nm², i.e., the density of carbon dimers on the reconstructed (100) surface. A 15 nm crystallite requires about 50 s (at 1 μm/h growth rate) to complete

Theoretical Studies on Nanocrystalline Diamond

J. Phys. Chem. B, Vol. 103, No. 26, 1999 **5465**

its growth while developing about 300 nm^2 of (100) surface for each grain. This grain size would give rise to a grain density of about 4×10^{11} grains/cm^2. Combining this with the nucleation site density of 8 sites/nm^2 (or equivalently about 2×10^3 sites/grain), we find that the maximum rate of creation of nucleation sites would be 2×10^{13} sites cm^{-2} s^{-1}, which is about 3 orders of magnitude higher than the experimentally determined nucleation rate of about 10^{10}/cm^2 s. Thus, in order for nucleation at unhydrided carbon dimers to account for experimental nucleation rates, at least 0.05% of surface carbon dimers must be unhydrided.

There are three possibilities for how secondary nucleation could proceed from further addition of C$_2$ to the carbene: growth of a one-dimensional chain, growth of a two-dimensional cluster such as a graphite-like sheet, and growth of a three-dimensional cluster such as a diamond or fullerene structure. Since calculations on the growth beyond the carbene are difficult, we can only speculate on the likelihood of each possibility. From calculations of carbon cluster energies, it is known that three-dimensional carbon clusters of the fullerene type do not become stable until the clusters contain more than about 25−30 atoms.[23] Diamond-like clusters do not become stable until even larger clusters sizes are attained. However, it is known from molecular dynamics simulations that once the new crystallite has formed, the grain boundaries are π-bonded,[2] consistent with our picture of the carbene on the unhydrided surface acting as a nucleation site. We now present the results of periodic density functional calculations of the geometry, energetics, and electronic structure of such a grain boundary.

V. Electronic Structure of a Diamond Planar Defect

If we assume that secondary nucleation is initiated by the insertion of dicarbon molecules into the dimer rows of a nonhydrogenated reconstructed (100) diamond surface, then a high concentration of inserted dicarbons could create a template for the growth of a new diamond crystallite with a planar defect, although the growth of a graphite-like phase is also possible. We assume that the resulting structures are two-dimensionally periodic in the surface plane. The simplest case of such a periodic defect structure is represented by two (100) diamond surfaces interconnected by dicarbon moieties aligned normal to the surface. Formally speaking, this defect is a stacking fault since it can be obtained by a translation of half of the perfect crystal parallel to the (100) surface. However, this is not the usual type of low-energy stacking fault characteristic of non-covalently bonded solids, because the coordination and bonding of atoms in the interfacial layer of diamond have changed drastically. It can be considered to be a model of a grain boundary that has predominantly sp^2-type bonding across the interface, in consonance with molecular dynamics simulations of grain boundaries in nanocrystalline diamond, which predict predominantly sp^2-type bonding in the interfacial region.[2]

To assess the suitability of the periodic density functional method for the present studies, we calculated several of the well-known physical properties of diamond and graphite. Optimized lattice constants for diamond (3.58 Å) and graphite (a = 2.47 Å and c = 6.71 Å) are in very good agreement with experiment (3.57 Å for diamond and a = 2.46 Å and c = 6.7 Å for graphite). It is worth noting that the graphite interlayer spacing is usually poorly reproduced in less sophisticated interatomic interaction models that are routinely used for grain boundary studies in diamond. We have calculated the difference between the total electronic energies of diamond and graphite to be 0.9 kcal/mol, with graphite being more stable. The experimental
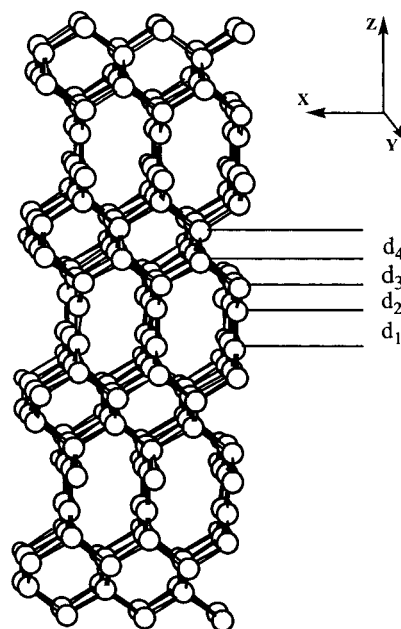

Figure 6. Geometry of a periodic planar defect in the diamond structure. Inequivalent distances between interface layers (d_1), between interface layer and second layer (d_2), and between the next two diamond layers (d_3 and d_4) are shown.

enthalpy of formation of diamond at 0 K is 0.6 kcal/mol. To directly compare theoretical and experimental results, the difference of zero-point energies for diamond and graphite should be subtracted from the enthalpy of formation of diamond at 0 K. By a crude estimate, the difference in Debye temperatures for the two phases is about 1000 K, which gives about a 2 kcal/mol difference in zero-point energies. Thus, the calculated total electronic energy difference of 0.9 kcal/mol can be compared to the estimate of −1.4 kcal/mol from experimental data. It is interesting to note that the zero-point vibrational contribution to the enthalpy of formation is crucial for stabilization of the graphite phase, without which diamond would be more stable.

As far as the electronic structure is concerned, we obtained the value of 4.1 eV for the fundamental energy gap of diamond. The position of the conduction band minimum is approximately $^3/_4$ of the way toward the X point in the Γ−X direction. The experimental indirect forbidden gap width is 5.45 eV, and the discrepancy with our result is attributable to the well-known deficiencies of the Kohn−Sham method for insulators. For graphite, our calculations produce zero band gap at the K-point, in agreement with other studies.[24] Having established that our computational methods produce a realistic description of the most stable solid carbon phases, we proceed with modeling planar defects in diamond.

The model comprises a six-layer slab periodically repeated in the z direction. The two innermost layers of the slab represent a (100) planar defect, which is separated by four layers of diamond from the next equivalent defect. The geometry of the system is shown in Figure 6. There are 12 atoms in the unit cell, only 3 of which are symmetry inequivalent. The positions of atoms in the xy plane were restricted, leaving three interplanar spacing parameters to be optimized: the distances between the two interface planes (d_1 in Figure 6), between the surface plane and the second diamond plane (d_2 in Figure 6), and between the second and third diamond planes (d_3 in Figure 6). The remaining interplanar spacing, d_4, was fixed at the bulk diamond value of 0.895 Å. The optimized values of these parameters are d_1 = 1.34 Å, d_2 = 0.828 Å, and d_3 = 0.918 Å. The distance
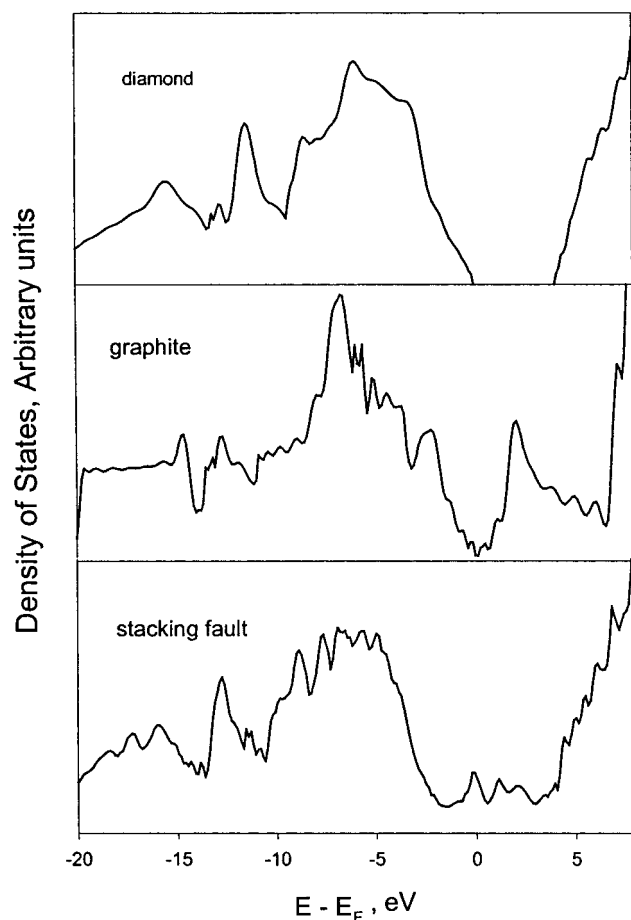
Figure 7. Total density of states plots for diamond, graphite, and diamond with periodic stacking faults.

Figure 8. Density of states projected on the s and p orbitals of the interface atom.

between interface atoms is smaller than that in graphite rings (1.42 Å) and the other interlayer distances are slightly different from the defect-free diamond interplanar spacing of 0.895 Å. The volume increase per unit surface area is $0.1a$, which can be compared to $0.11a$ obtained from atomistic simulations of twist grain boundaries in diamond.[25] As far as the system energetics is concerned, the formation energy for one interface atom is 0.84 eV. The defect energy per surface area, 4.2 J/m^2, compares favorably to twist grain boundary energies in diamond, which are typically 2−7 J/m^2.[2,25] The electronic structure of the diamond crystal with defects exhibits a marked difference from both diamond and graphite electronic structures. Total density of states plots for diamond, graphite, and our model of diamond with defects are shown in Figure 7. Each plot is normalized by the number of carbon atoms in the respective unit cell. No smoothing or thermal broadening have been applied. The density of states for diamond with defects is similar to that for bulk diamond everywhere except the diamond band gap region. Peaks that are similar to graphite π-states appear in the band gap. As a result, the valence and conduction energy bands slightly overlap. The height of the peaks is strongly dependent on the concentration of planar defects. Since our model has an extremely high defect concentration (one interface atom per two bulk atoms), it is expected that the density of states in the energy gap of real nanocrystalline material should be several times lower.

The appearance of defect states in the fundamental gap of diamond is attributed to the electronic states of atoms in the interfacial layer. The density of states projected on s and p orbitals of these atoms is sho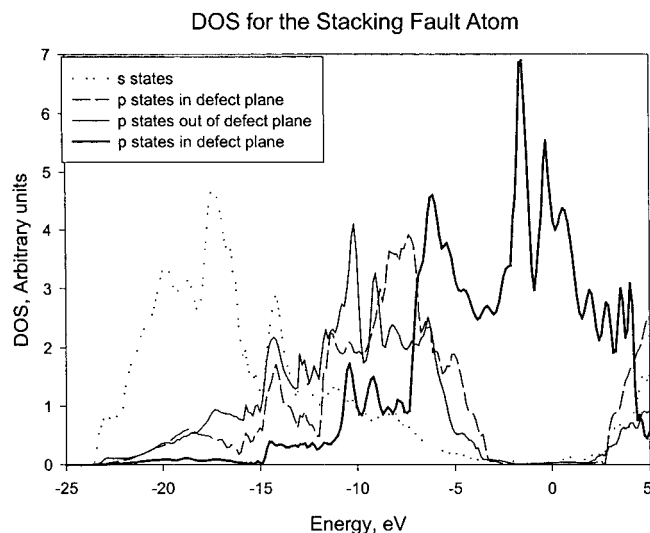wn in Figure 8. It appears that neither σ-bonds across the interface nor σ-type back-bonds between interface atoms and next layer atoms introduce any states in the forbidden gap. All three σ-bonds of the interfacial carbon atom are formed as a result of sp^2 hybridization. The π-states formed by p-orbitals lying in the defect plane introduce energy bands in the forbidden gap that essentially lead to the absence of the forbidden gap in the crystal with defects. The three most prominent peaks were found at −0.1, 1.1, and 2.1 eV with respect to the Fermi level. It should be noted that a mechanism for the grain boundary conductivity can be proposed on the basis of the presence of such states in the grain boundary electronic structure. There is still a question about the nature of such a mechanism since sp^2-bonded carbons do not form a continuous network. A hopping mechanism for grain boundary conductivity was recently suggested.[26] We note that the states at the top of the valence band belonging to four-coordinated diamond-like atoms are very close in energy to the unoccupied states of sp^2-bonded atoms. This consideration leads to another possible mechanism of grain boundary conductivity involving atoms in the interfacial layer and the next diamond-like layer that together to form a continuous path along the interface. Such a mechanism involves site-to-site electron transfer between electronic states of atoms with different coordination.

Next, we would like to highlight the similarities and differences between our defect model and a real grain boundary. We assume, on the basis of previous studies, that a majority of the interface atoms have double bonds across the grain boundary. For instance, tight-binding molecular dynamics studies of a Σ5 twist grain boundary in diamond conclude that almost all atoms in the interface are connected by double bonds, and results for Σ29 indicate that 80% of the atoms are sp^2 bonded in the interface region.[2] Thus, our model correctly describes the system in this respect. As far as bond orientation in the interface plane is concerned, twist grain boundaries do not have preferential orientation of bonds in the plane, whereas our model has all the π-bonds oriented in the same direction. Therefore, it is not possible to strictly separate σ-states and π-states in the electronic structure for a realistic twist grain boundary. Nevertheless, it does not change the conclusion that the electronic states localized in the interfacial plane will be the ones that are responsible for defect states in the fundamental gap of the crystal.

Rotation and deformation of the bonds may lower the grain boundary formation energy since a large part of it comes from
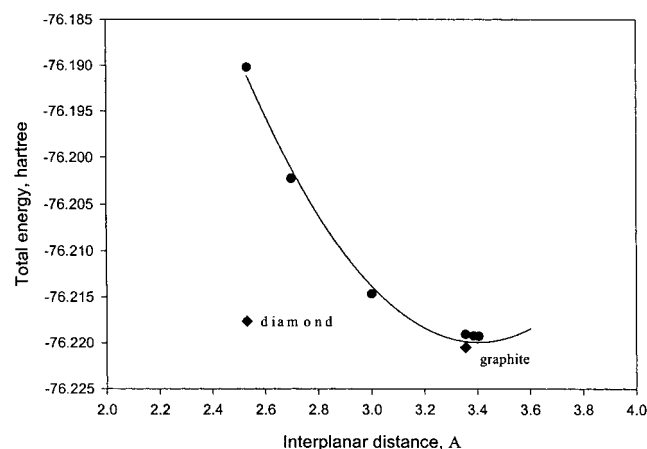
Theoretical Studies on Nanocrystalline Diamond

J. Phys. Chem. B, Vol. 103, No. 26, 1999 **5467**

Figure 9. Total energy per unit cell versus interlayer distance for hexagonal graphite in AA stacking. Energies of diamond and graphite are given for comparison.

the repulsion between too closely spaced π-bonds. They are forced to maintain the same distance of 2.53 Å as atoms in the diamond (100) plane. This repulsion is the reason growth of graphite-like layers normal to the surface plane proposed in some previous studies[27] is highly unlikely. Indeed, interlayer spacing in graphite is much larger, and compressing it to 2.53 Å is energetically unfavorable. To clarify this point, we have calculated the total energy per atom of hexagonal graphite in AA stacking sequence as a function of interlayer distance (see Figure 9). The difference in binding energy per carbon atom between uncompressed and uniaxially compressed (to 2.53 Å) graphite is 0.41 eV. It is likely that such a compression of graphite sheets will result in a phase transition into a more stable phase. As a result of the large lattice mismatch between graphite and diamond, growth of parallel graphene sheets normal to the diamond (100) surface is not plausible. This conclusion is corroborated by experimental TEM evidence of grain boundary thicknesses of the order of 1−2 monolayers in nanocrystalline diamond.[28]

VI. Conclusions

We have presented results of a density functional and ab initio molecular orbital theory study of the energetics of C_2 insertion into C_9H_{12} and C_9H_{14} clusters that model the unhydrided and monohydrided (100) surfaces, respectively. These results suggest that the mechanism of diamond growth from dicarbon may be dependent on the degree of hydrogenation of the reconstructed (100) surface. On the unhydrided surface, the insertion of C_2 into a C=C bond produces a carbene, while on the monohy-drided surface, the insertion of C_2 into C−H bonds to form a cyclobutene-like structure is favored. The carbene on the unhydrided surface may act as a nucleation site for a new diamond crystal, but on the monohydride surface, the growth of the existing crystal proceeds readily from the cyclobutene structure. The disparate nucleation rates of diamond crystallites grown in hydrogen-rich versus hydrogen-poor microwave plasmas may be accounted for qualitatively by these results.

Periodic density functional calculations of a high-energy planar defect in diamond adequately reproduce the properties of (100) twist grain boundaries. The formation energy of the π-bonded planar defect is 4.2 J/m^2. The electronic structure of diamond with defects is characterized by the presence of π-states in the forbidden gap that are localized on the interfacial atoms. These states produce several broad peaks in the gap and play a

key role in the grain boundary conductivity. The defect region is very thin, having a thickness of one to two atomic layers. Formation of larger graphitic regions normal to the interface is shown to be energetically unfavorable due to a large lattice mismatch between graphite and diamond.

References and Notes

(1) Gruen, D. M.; Krauss, A. R.; Zhou, D.; McCauley, T. G.; Corrigan, T. D.; Chang, R. P. H.; Swain, G. M. *Electrochem. Soc. Proc.* **1997**, *97*−*25*, 325.

(2) Keblinski, P.; Wolf, D.; Phillpot, S. R.; Gleiter, H. *J. Mater. Res.* **1998**, *13*, 2077.

(3) Zuiker, C.; Krauss, A. R.; Gruen, D. M.; Pan, X.; Li, J. C.; Csencsits, R.; Erdemir, A.; Bindal, C.; Fenske, G. *Thin Solid Films* **1995**, *270*, 154.

(4) Zhou, D.; Gruen, D. M.; Qin, L. C.; McCauley, T. G.; Krauss, A. R. *J. Appl. Phys.* **1998**, *84*, 1981.

(5) Gruen, D. M. *MRS Bull.* **1998**, *23* (9), 32.

(6) Goyette, A. N.; Lawler, J. E.; Anderson, L. W.; Gruen, D. M.; McCauley, T. G.; Zhou, D.; Krauss, A. R. *Plasma Sources Sci. Technol.* **1998**, *7*, 149. Goyette, A. N.; Lawler, J. E.; Anderson, L. W.; Gruen, D. M.; McCauley, T. G.; Zhou, D.; Krauss, A. R. *J. Phys. D* **1998**, *31*, 1975.

(7) Horner, D. A.; Curtiss, L. A.; Gruen, D. M. *Chem. Phys. Lett.* **1996**, *223*, 243.

(8) Redfern, P. C.; Horner, D. A.; Curtiss, L. A.; Gruen, D. M. *J. Phys. Chem.* **1996**, *100*, 11654.

(9) Lusie, P. G.; Wilson, J. M. *Surf. Sci.* **1977**, *65*, 453. Shiami, H.; Tanabe, K.; Fujimori, N. *Jpn. J. Appl. Phys.* **1990**, *29*, 34. Tsuno, T.; Imai, T.; Nishibayashi, Y.; Hamada, K.; Fujimori, N. *Jpn. J. Appl. Phys.* **1990**, *30*, 1063.

(10) Thoms, B. D.; Butler, J. E. *Surf. Sci.* **1995**, *328*, 291.

(11) Hehre, W. J.; Radom, L.; Pople, J. A.; Schleyer, P. v. R. *Ab Initio Molecular Orbital Theory*; Wiley: New York, 1987.

(12) Frisch, M. J.; Trucks, G. W.; Schlegel, H. B.; Gill, P. M. W.; Johnson, B. G.; Robb, M. A.; Cheeseman, J. R.; Keith, T.; Petersson, G. A.; Montgomery, J. A.; Raghavachari, K.; Al-Laham, M. A.; Zakrzewski, V. G.; Ortiz, J. V.; Foresman, J. B.; Cioslowski, J.; Stefanov, B. B.; Nanayakkara, A.; Challacombe, M.; Peng, C. Y.; Ayala, P. Y.; Chen, W.; Wong, M. W.; Andres, J. L.; Replogle, E. S.; Gomperts, R.; Martin, R. L.; Fox, D. J.; Binkley, J. S.; Defrees, D. J.; Baker, J.; Stewart, J. P.; Head-Gordon, M.; Gonzalez, C.; Pople, J. A. *Gaussian 94*; Gaussian, Inc.: Pittsburgh, 1995.

(13) Kohn, W.; Becke, A. D.; Parr, R. G. *J. Phys. Chem.* **1996**, *100*, 12874.

(14) Curtiss, L. A.; Raghavachari, K.; Trucks, G. W.; Pople, J. A. *J. Chem. Phys.* **1991**, *94*, 7221.

(15) Dovesi, R.; Saunders, V. R.; Roetti, C.; Causa, M.; Harrison, N. M.; Orlando, R.; Apra, E. *CRYSTAL95 User's Manual*; University of Torino: Torino, 1996.

(16) Becke, A. D. *Phys. Rev. A* **1988**, *38*, 3098.

(17) Perdew, J. P.; Wang, Y. *Phys. Rev. B* **1986**, *33*, 8800. Perdew, J. P.; Wang, Y. *Phys. Rev. B* **1989**, *40*, 3399. Perdew, J. P.; Wang, Y. *Phys. Rev. B* **1989**, *45*, 13244.

(18) Skell, P. S.; Jackman, L. M.; Ahmed, S.; McKee, M. L.; Shelvin, P. B. *J. Am. Chem. Soc.* **1989**, *111*, 442.

(19) Johnson, R. P.; Daoust, K. J. *J. Am. Chem. Soc.* **1995**, *117*, 362.

(20) Fitzgerald, G.; Saxe, P.; Schaefer, H. F., III *J. Am. Chem. Soc.* **1983**, *105*, 690.

(21) Skokov, S.; Weiner, B.; Frenklach, M. *J. Phys. Chem.* **1995**, *99*, 5616.

(22) Badzian, A. R.; De Vries, R. C. *Mater. Res. Bull.* **1988**, *23*, 385.

(23) Feyereisen, M.; Gutowski, M.; Simons, J.; Almlöf, J. *J. Chem. Phys.* **1992**, *96*, 2926.

(24) Boettger, J. C. *Phys. Rev. B* **1997**, *55*, 11202.

(25) Wang, Z. Q.; Dregia, S. A.; Stroud, D. *Phys. Rev. B* **1994**, *49*, 8206.

(26) Cleri, F.; Keblinski, P.; Colombo, L.; Wolf, D.; Phillpot, S. R. *Phys. Rev. Lett.*, submitted.

(27) Shenderova, O.; Brenner, D. W. *Mater. Res. Soc. Symp. Proc.* **1997**, *442*, 693.

(28) Qin, L. C.; Zhou, D.; Krauss, A. R.; Gruen, D. M. *Nanostruct. Mater.* **1998**, *10*, 649.